HHS Public Access

Author manuscript

Kidney Int. Author manuscript; available in PMC 2016 August 01.

Published in final edited form as:

Kidney Int. 2016 February ; 89(2): 498–505. doi:10.1038/ki.2015.316.

Phenotyping by magnetic resonance imaging nondestructively measures glomerular number and volume distribution in mice with and without nephron reduction

Edwin J. Baldelomar, B.Sc.[1a,c], **Jennifer R. Charlton, M.D., M.Sc.**[2], **Scott C. Beeman, Ph.D.**[3], **Bradley D. Hann, B.Sc.**[1b,c], **Luise Cullen-McEwen, Ph.D.**[3], **Valeria M. Pearl, B.Sc.**[2], **John F. Bertram, Ph.D.**[4], **Teresa Wu, Ph.D.**[5], **Min Zhang, Ph.D.**[5], and **Kevin M. Bennett, Ph.D.**[1c]

[1a]University of Hawaii at Manoa, Department of Physics, Honolulu, Hawaii, USA

[1b]University of Hawaii at Manoa, Department of Molecular Biosciences and Bioengineering, Honolulu, Hawaii, USA

[1c]University of Hawaii at Manoa, Department of Biology, Honolulu, Hawaii, USA

[2]University of Virginia, Charlottesville, Virginia, USA

[3]Washington University School of Medicine, Saint Louis, Missouri, USA

[4]Monash University, Clayton, Victoria, Australia

[5]Arizona State University, Tempe, Arizona, USA

Abstract

Reduced nephron mass is strongly linked to susceptibility to chronic renal and cardiovascular diseases. There are currently no tools to identify nephropenia in clinical or preclinical diagnostics. Such new methods could uncover novel mechanisms and therapies for chronic kidney disease (CKD) and reveal how variation among traits can affect renal function and morphology. Here we used cationized ferritin (CF) enhanced-MRI (CFE-MRI) to investigate the relationship between glomerular number (*Nglom*) and volume (*Vglom*) in kidneys of healthy wild type mice and mice with oligosyndactylism (Os/+), a model of congenital nephron reduction. Mice were injected with cationic ferritin and perfused and the resected kidneys imaged with 7T MRI to detect CF-labeled glomeruli. CFE-MRI was used to measure the intrarenal distribution of individual glomerular volumes and revealed two major populations of glomeruli distinguished by size. Spatial mapping revealed that the largest glomeruli were located in the juxtamedullary region in both wild type and Os/+ mice and the smallest population located in the cortex. Os/+ mice had about a 50% reduction and 35% increase of *Nglom* and *Vglom*, respectively, in both glomerular populations compared to wild type, consistent with glomerular hypertrophy in the Os/+ mice. Thus, we provide a

*Address correspondence to: Kevin M. Bennett, PhD, Department of Biology, University of Hawaii at Manoa, 2540 Campus Rd. Honolulu, HI. 96822, ; Email: kevinben@hawaii.edu

DISCLOSURE

Kevin M. Bennett owns Nanodiagnostics LLC.

foundation for whole-kidney, MRI-based phenotyping of mouse renal glomerular morphology and provide new potential for quantitative human renal diagnostics.

Keywords

kidney; nephron endowment; magnetic resonance imaging; glomerular number; nephropenia; Os/+; transgenic mouse; nephropenia

INTRODUCTION

Nephropenia is strongly associated with susceptibility to chronic kidney disease (CKD) and cardiovascular disease[1–4]. While nearly 26 million American adults suffer from CKD[5], there is no effective tool to detect low nephron endowment or nephron loss at the earliest stages. Renal adaptation to low nephron endowment can lead to compensatory glomerular and tubular hypertrophy. The cyclic perpetuation of hyperfiltration and adaption ultimately leads to progressive renal damage, evidenced by an inverse correlation between glomerular number and volume observed post-mortem in humans and rodents[1,6]. There are many clinical applications in which knowledge of a patient's nephron number (N_{glom}) and volume (V_{glom}) could impact clinical care or influence medical decision-making, for example in evaluation of renal allograft donation, renal assessment following acute kidney injury or preclinical evaluation of renal toxicity of new therapeutics. The inability to measure N_{glom} and V_{glom} also extends to preclinical models as there is no tool to monitor nephron number or renal response to reduced nephron number. Such tools could uncover novel mechanisms and therapies for CKD and reveal how variation of traits affects renal function and morphology.

Acid maceration and stereology are the predominant methods to assess N_{glom} and V_{Glom},[7,8] and have had a fundamental impact on the understanding of kidney development, health, and disease. However, histological approaches are limited to post-mortem analysis after destruction of the kidney, do not allow for longitudinal analysis, and do not easily allow three-dimensional (3D) visualization and integration of the renal microstructure.

Preclinical models using transgenic or genetically altered animals are critical to understanding the pathogenesis of renal disease. But there have been few studies that quantify nephron morphology and variation in rodents. Magnetic resonance imaging (MRI) is gaining interest for renal phenotyping because it is noninvasive and can potentially be performed *in vivo*[9]. Such a tool would be valuable beyond transgenic mouse models to animal models of nephrotoxicity, ischemia, diabetes, and obesity[10].

There has been increased interest recently in the development of imaging tools to probe microstructure with MRI[11,12]. Recently, a cationized form of ferritin (the predominant mammalian iron-storage protein) has been developed as a contrast agent for MRI to measure kidney glomerular morphology[10,13–17]. Ferritin forms a ~13 nm nanoparticle with a metal oxide core. Cationic ferritin (CF) is functionalized with amines[18] and has an isoelectric point of up to ~9[13]. After intravenous injection, CF nanoparticles bind to anionic proteoglycans in the glomerular basement membrane (GBM). The iron oxide core of the CF nanoparticles is

detected by T_2*-shortening in MRI that produces a dark punctate artifact at the site of CF accumulation[13]. CF-enhanced MRI (CFE-MRI) has enabled measurements of N_{glom} and V_{glom} in intact isolated rat kidneys *ex vivo*[14,15] and in isolated human donor kidneys[19]. CFE-MRI has also been used to image nephrons *in vivo* in rats[13,17,20].

Here we used CFE-MRI to generate 3D-maps of perfused glomeruli and measure N_{glom}, and V_{glom} in healthy, mouse kidneys *ex vivo*. We further applied CFE-MRI to investigate the oligosyndactylism (Os/$^+$) mouse model of congenital nephron reduction, to determine how N_{glom} and V_{glom} are affected by reduced renal mass. The Os/$^+$ mouse has a mutation on chromosome 8 secondary to radiation exposure with two dominant phenotypic manifestations including (1) fusion of the second and third digits on each limb and (2) reduced nephron number[21–25]. Homozygous inheritance results in death shortly after implantation[26–29]. The Os/$^+$ mutation disrupts *Anapc10*, which encodes for component 10 of the anaphase-promoting complex/cyclosome (APC/C). Although there is a human ortholog to this gene (*ANAPC10*) which resides on chromosome 10, there is no prior report of a mutation in vertebrates[30].

We compared MRI-based measurements to histological estimates and investigated the intra- and inter-renal distribution of IGV. This work provides the foundation for whole-kidney, MRI-based phenotyping of mouse renal glomerular morphology.

RESULTS

We imaged 10 CF-labeled (5 WT, 5 Os/$^+$) and two unlabeled mouse kidneys with 7T MRI using a 3D gradient recalled echo (GRE) pulse sequence. MR images (Figure 1-a) of CF-labeled kidneys exhibited dark spots in the cortex, consistent with accumulation of CF in individual glomeruli[13,14,19]. Images of the kidneys from unlabeled mice exhibited no spots[13,14]. Binding of CF to the GBM was confirmed with immunofluorescence in WT and Os/$^+$ mice, as shown in Figure 2.

We segmented each kidney from original 3D MR images. Our custom software identified CF-labeled glomeruli from the 3D MR images and measured the number of labeled glomeruli in each kidney. We segmented glomeruli and cortex in optical images and used histological methods to estimate N_{glom} and V_{glom} (Figure 3). MRI-based measurements yielded an average N_{glom} of 12 010 ± 447 (WT) and 5 632 ± 1 279 (Os/$^+$). Stereological estimates yielded average N_{glom} of 11 660 ± 1 091 (WT) and 5 561 ± 1 954 (Os/$^+$). Acid maceration estimates of average N_{glom} were 10 364 ± 1 123 (WT) and 4 281 ± 655 (Os/$^+$). Unlabeled kidneys imaged with MRI gave an average count of 1 075. The average Dice coefficient for WT and Os/+ kidneys was 0.945, indicating that MRI-based detection was robust. Original MR images of kidneys in a multi-kidney holder and corresponding identification (ID) maps are shown in Figure 1.

The perturbation caused by CF labeled glomeruli in MRI extended several voxels, as seen in Figure 4-a. We calculated V_{glom} in each kidney using line profiles applied in 3D to identified glomerular voxels in MRI. Mean-V_{glom} values using (a.) 50% (b.) 55% (c.) 60% and (d.) 75% of the mean profile height were: (a.) 3.281 and 3.910 (b.) 2.671 and 3.065 (c.) 2.057

and 2.431 (d.) 0.850 and 1.010, (10^{-4} mm^3) in WT and Os/$^+$ mice, respectively. V_{glom} measured at 55% of profile height matched most closely with stereological estimates with a 9.8/20.8 % difference in WT/Os/$^+$, respectively. V_{glom} calculated from MR line profiles, 2.684 ± 0.324 (WT) and 3.176 ± 0.280 (Os/$^+$), compared well with stereological estimates of V_{glom}, 2.433 ± 0.219 (WT) and 3.871 ± 0.724 (Os/$^+$), 10^{-4} mm^3. One outlier Os/$^+$ kidney had a N_{glom} and V_{glom} that deviated significantly from the other Os/$^+$ kidneys. There was no correlation of N_{glom} or V_{glom} with either kidney weight or volume in WT or Os/+ mice. N_{glom} and V_{glom} from MRI and histology and corresponding kidney weights and volumes are shown in Figure 5-a. The relationship of V_{glom} with N_{glom} is plotted in Figure 5-b using MRI and stereology. Line profile formation and IGV distributions for WT and Os/$^+$ kidneys are illustrated in Figure 4.

We compared the distribution of IGV in WT and Os/$^+$ kidneys from MRI. Both groups exhibited apparently bimodal distributions of IGV with one small population ($V_{G\text{-}Low}$) and a second larger population ($V_{G\text{-}High}$). A double Gaussian model was consequently fitted to each distribution. We measured the full width at half max (FWHM) of each distribution and found that $V_{G\text{-}High}$ in Os/$^+$ kidneys had a 20% greater FWHM and mean compared to WT. $V_{G\text{-}Low}$ was 5% higher in FWHM and 2% lower in the mean in Os/$^+$ kidneys compared to WT. Size distribution and relationship to N_{glom} are shown in Figure 6. The increase in FWHM of $V_{G\text{-}High}$ is attributed to a larger fraction of glomeruli with larger volumes in Os/$^+$ mice compared to WT.

Confocal images and MRI revealed a spatial distribution of profile areas of glomeruli. We measured a 14% larger average profile area and a 60% higher standard deviation of profile area for Os/$^+$ mice compared to WT. Color maps of glomerular profile area are overlaid on confocal and MRI images in Figure 7 along with MRI volume profiles. Larger glomeruli were mostly juxtamedullary, with more large glomeruli visible in Os/$^+$ kidneys. IGV correlated ~60% with a polynomial fit to the profile area of the same glomerulus; thus the spatial distribution of IGV was consistent with the distribution of glomerular areas.

We examined how N_{glom} and V_{glom} co-varied between MRI and stereology. V_{glom} decreased with increasing N_{glom}. We observed a linear correlation between MRI and stereology for $N_{glom\text{-}Os/+}$, $V_{glom\text{-}WT}$, $V_{glom\text{-}OS/+}$ but not for $N_{glom\text{-}WT}$. The correlation coefficients between MRI and stereology for N_{glom} and V_{glom} were 0.67/−0.12 and 0.59/0.31 (Os/$^+$/WT), respectively. There was no significant difference in N_{glom} and V_{glom} between MRI and stereology ($\alpha = 0.05$, $p_{Nglom} = 0.55$, $p_{Vglom} = 0.28$). There was a significant difference between MRI and acid maceration ($\alpha = 0.05$, $p_{Nglom} = 0.006$).

DISCUSSION

This work demonstrates the nondestructive measurement of mouse kidney N_{glom}, V_{glom}, and IGV distribution with MRI in healthy and mice with reduced nephron number. CFE-MRI provides a unique view of renal phenotype and morphology, allowing for spatial mapping of each perfused glomerulus.

CFE-MRI revealed morphological differences in glomeruli between Os/$^+$ and WT mice. MRI-based measurements of N_{glom} and V_{glom} were consistent with those obtained from stereology and acid maceration. N_{glom} reported here was ~14% less than previous literature reports in Os/$^+$ mice[24]. This may be due to genetic heterogeneity in the Os/$^+$ strain. We also detected increased V_{glom} in Os/$^+$ kidneys with MRI, consistent with glomerular hypertrophy.

Intra-renal measurements of IGV uncovered two major populations ($V_{G\text{-}High}$ and $V_{G\text{-}Low}$) of glomerular sizes in kidneys. $V_{G\text{-}High}$, $V_{G\text{-}Low}$, and composite distribution varied with nephron endowment. CFE-MRI also identified one Os/$^+$ outlier and had a low standard deviation in N_{glom} compared to stereology, confirming the robustness of CFE-MRI.

In CFE-MRI, CF accumulation and IGV are detected through the size of the perturbation in the magnetic field in and around the glomerulus. This perturbation may be detected within a single voxel or across multiple voxels, depending on the image resolution, glomerulus size, and amount of CF in the glomerulus. Consequently, validation with stereology was critical. Based on CF relaxivity, we estimate that glomeruli ~40 um in diameter or smaller would not be detected using the current resolution. Similarly, glomeruli ~80 um in diameter labeled with ~40% less CF would not be likely detected. Nonetheless, CFE-MRI yielded an excellent match to N_{glom} and V_{glom} obtained from histology.

We observed a distribution of glomerular sizes, with a larger population of glomeruli appearing primarily in the juxtamedullary region of the kidney. Previous work in C57/BL/6J mouse kidneys also revealed a range of estimated glomerular volumes based on location within the kidney, with up to a 200% greater IGV in juxtamedullary glomeruli[31]. These prior methods were limited by small numbers of glomeruli sampled. With CFE-MRI it is possible to identify all perfused glomeruli in the kidney. The range of IGV measured with CFE-MRI is also consistent with previous measurements [31]. We suspect that the spatial distribution of IGV may reflect the proximity of the juxtamedullary glomeruli to larger vessels under higher pressure.

Future work will focus on estimating nephron endowment and function *in vivo*. Nephrons can be detected *in vivo* with CFE-MRI[13] and Qian, et al. have recently developed a wireless radiofrequency amplifier that allows local visualization of individual glomeruli in the rat kidney *in vivo*[17,20]. Modification of the ferritin metal core will also improve the detection of glomeruli *in vivo*[32]. Exploring such new agents while improving acquisition time will enable application of CFE-MRI for whole kidney nephron measurements, *in-vivo*.

Preliminary toxicology studies have demonstrated the potentially safe use of CF in rats at MRI-detectable doses[16]. In mice, intravenous injections of CF do not perturb kidney or liver function[16,33]. Further work is required to determine the potential toxicity of nanoparticles of this charge or iron load in mouse models of disease. CF is rapidly metabolized in rodents with no MRI evidence in the kidney by 2 days or liver by 7 days[16,34]. In preliminary, unpublished data from our group, there is no histologic evidence of horse spleen ferritin in the mouse kidney, liver, spleen or lung 3 weeks after injection of CF with mild iron accumulation in the spleen.

In disease models it is important to consider the effect of glomerular charge barrier disruption on CF accumulation. We have applied CFE-MRI to investigate a puromycin (PAN)-induced model of focal and segmental glomerulosclerosis (FSGS) in the rat[35]. One major feature of PAN-induced FSGS is podocyte effacement, a common hallmark of human glomerular disease usually associated with GBM charge barrier disruption[36]. In early and late-stage FSGS there was decreased focal labeling of glomeruli and increased darkening of surrounding tissue in the cortex. In early stages of FSGS, the glomeruli were readily identified by MRI. By late stage, CF was detected throughout the cortex. Immunoflourescence and electron microscopy at late-stage-FSGS revealed internalization of CF by podocytes and almost no labeling of CF on the GBM. This is consistent with GBM disruption known to occur in FSGS and indicates a redistribution of CF from the GBM into the cell body after GBM breakdown. While GBM charge barrier destruction may limit measurements of N_{glom} and V_{glom} in severe glomerular disease, this redistribution of CF may be a valuable marker for morphological damage and a probe for correlation between nephron structure and function.

Here we reported several technical improvements over our previous work in CFE-MRI[14]. We employed high-throughput imaging of multiple kidneys, segmenting them with postprocessing to reduce total acquisition time. The total time from the start of the MRI study (first injection) to final measurements of N_{glom} and V_{glom} in all mice was less than 48 hours.

We observed that V_{glom} and N_{glom} are coupled in the Os/$^{+}$ model of nephron reduction, and report a redistribution of IGV in these mice, likely due to hypertrophy. With a desperate need for improved clinical renal diagnostics and significant reliance on transgenic mouse models employed in kidney research, renal phenotyping in mice by CFE-MRI may prove vital to basic kidney research, opening the door to new diagnostics and therapies.

METHODS

Animal preparation and MRI

Animal experiments were approved by the University of Virginia (UVa) Institutional Animal Care and Use committee and were performed in accordance with the NIH Guide for the Care and Use of Laboratory Animals. C57Bl/6 mice were bred at UVa. Adult Os/$^{+}$ males, bred on a predominantly C57Bl/6 background, were identified by syndactylism of their toes.

We used MRI to examine the kidneys of five healthy wild type (WT) mice (~20 g) and five Os/$^{+}$ mice (~20g) intravenously injected with CF. All mice received a total of 5.75 mg/100g-body-weight of commercial CF (Sigma Aldrich, St. Louis, MO) administered under isoflurance gas anesthesia to effect in two retro-orbital injections separated by 1.5 h. Two more WT mice received no CF as controls. All mice were sacrificed 1.5 h after the last injection by CO_2 inhalation. Left kidneys were clamped and mice were perfused transcardially. Kidneys were then resected. The left kidney was stored in saline solution at 4°C for acid maceration and the right in a 2% glutaraldehyde/0.1 M cacodylate solution at 4°C for imaging. Right kidneys were placed together in a plastic cylindrical tube with the cacodylate solution and imaged with MRI using a 3D gradient recalled echo (GRE) pulse

sequence. A linearly polarized RF coil (inner core diameter = 15 mm) (Bruker, MA, USA), tuned and matched to 300 MHz, was used with a Bruker 7T/30 MRI (Bruker, MA, USA), (TE/TR = 20/80 ms, resolution (X, Y, Z) = 50 × 50 × 55 μm^3). After MRI, right kidneys were evaluated by immunohistochemistry and stereology.

Image processing

Kidneys were first segmented from the original 3D image. Individual kidney segmentation and masking was performed with MATLAB (The Mathworks, Inc., MA, USA), using built in 'roipoly' function, and Amira software (FEI Visualization Sciences Group, France). CF-labeled glomeruli were counted using custom software in MATLAB.

To measure N_{Glom}, the 3D MR magnitude images were normalized from 0 to 1 and resized with 3D bi-cubic interpolation.Final dimensions were increased to five times the original resolution in the XY-directions and two times in the Z-direction (*XY is defined as the plane orthogonal to the main B_0 field along Z)*. Resampled resolution was .0102 × .0102 × .0275 μm^3. The magnitude of the image was then inverted in each pixel, and every pixel over 100 (background noise) was set to 100. Spatial gradients over XY (between two voxels) were calculated to define boundaries with large magnitude differences. The gradient was subjected to a binary threshold of g_{7T} = 1.6 where all pixels below the threshold were set to zero and all pixels equal to and above were set to value '1'. Regional minima, (or minima below S × [global maximum magnitude]), were located within suspected glomeruli and a guided watershed algorithm was used to identify true glomeruli based on local minimum. Glomeruli were counted in 3D using MATLAB's Connected Components function.

We used the Sorenson-Dice method, or Dice coefficient, to quantify how well our segmentation algorithm identified glomeruli[37]. We compared the number of manually-identified and computer-identified glomeruli in 30 slices, or 15%, of the imaged volume from two of the WT and two of the Os/+ mice. In all cases, sampled volumes were taken from similar areas of the kidney. We computed the DICE coefficient by $C_{DICE} = 2*C/(A+B)$, where C is the number of manually identified and automatically identified glomeruli that coincided. A and B are the number of glomeruli identified manually in MRI and the number of glomeruli identified by the algorithm, respectively.

Individual glomerular volume (IGV) was measured using line profiles drawn through each identified glomerulus. First, the voxel with the minimum magnitude was found for each glomerulus. A line profile was drawn automatically in a single direction, (here the x-direction relative to B_0), with 11 voxels from both sides of the minimum (23 total points). Each profile was normalized to the background tissue (here, two voxels of highest magnitude in the line profile). IGV was estimated from the line profile width assuming that glomeruli were spherical. This was considered reasonable given the resolution of MRI compared to the size of the glomerulus. We used 50%, 55%, 60% and 75% of total height (full width of profiles, FWP) to calculate IGV in each kidney and took the mean to define V_{Glom}. We compared MRI-based measurements of V_{glom} to all histology estimates. Finally, we computed the intra-renal distribution of IGV. We examined glomerular area profiles to compare with the area profiles identified in optical microscopy. We then compared the area profiles from MRI to the volumes of the same glomeruli that were measured in 3D. We

performed a cross-correlation of the glomerular area profiles to the volumes of the same individual glomerulus with a second-order polynomial fit using Matlab.

Validation

(a.) Stereology—We compared N_{glom} and V_{glom} measured with MRI to those measured by stereology of the same kidneys. Fixed kidneys were embedded in 15% gelatin (300 bloom). Gelatin blocks were fixed overnight in formalin, and then 75μm sagittal sections were cut with a vibrating blade microtome (Leica VT1000 S, Leica Biosystems). Kidneys were exhaustively sectioned. Every 8th slice was collected and placed in a bath of phosphate buffered saline (PBS). The first section was randomly chosen from an interval 1–7. Collected sections were blocked in PBS + 2% Bovine Serum Albumin (BSA) + 1% Triton X-100 (Sigma-Aldrich, St Louis, MO). They were then stained overnight in a dark room using wheat germ agglutinin conjugated to Alexa-555 (WGA-555; Life Technologies) at 1μg WGA per 1mL PBS + 0.1% BSA. After washing 3x in 0.01 M PBS + 0.1% BSA, tissue was mounted on slides using ProLong Diamond + DAPI, (Life Technologies). Images were acquired on a Zeiss (Zeiss, Germany) LSM 710 confocal microscope and 20x magnification (Resolution = 0.83 × 0.83 × 2 um). The Zeiss Zen software applied filters and emission ranges for Alexa-555.

Amira was used to segment cortex, medulla, and glomerular profiles in each image. Volume densities (V_V) of glomeruli and cortex were defined assuming that object profile area densities (A_A) in a 2D slice are equal to the whole object volume densities, $A_A = V_V$[38]. The number of glomeruli per cortex section (N_A) was estimated with the model-based approach of Weibel-Gomez (WG)[39,40]. WG has been validated to accurately estimate N_{glom} compared to the dissector/fractionator method in adult mice41. The number of glomeruli per total volume (N_V) was calculated using the formula $N_V = k/\beta \times N_A^{1.5}/V_V^{0.5}$ with constants k = 1.04 and β = 1.38 [38,42]. Cortical volume (V_{Cortex}) was assessed from segmentation of 3D-MRI images based on the difference in image magnitude between cortex and medulla. The number of glomeruli per kidney (N_{Glom}) was calculated by $N_{glom} = N_V \times V_{Cortex}$. V_{glom} was calculated by $V_{glom} = (V_{glom}/V_{Kidney}) / (N_{Glom}/V_{Kidney})$[43] with V_{glom}/V_{Kidney} defined as V_V and the relation $A_A = V_V$. We compared the maximum dimensions in X and Y of similar slices in MRI and stereology for each kidney to determine the percent of tissue shrinkage.

(b.) Acid Maceration—We performed acid maceration and counting as described previously[44] to further validate the MRI-based counts. Contralateral kidneys were cut into 1mm^3 pieces and incubated in 5 ml of 6 N HCl for 1.5 hrs. Pieces were crushed with a glass rod and strained with a pipette and diluted to 30 ml with water. Glomeruli were counted in a 35 mm culture dish with 1 mm^2 traces and N_{glom} in each kidney was estimated by average number of glomeruli per trace.

Immunofluorescence

Immunofluorescence was performed on formalin-fixed tissue after MRI and stereological analysis to confirm labeling of CF in the kidney. Tissue samples were embedded in paraffin and sectioned to 4-μm thickness. Sections were rehydrated using Histoclear (National Diagnostics, GA, USA), followed by serially decreasing ethanol dilutions. Sections were

then subjected to antigen retrieval, using a 10 mM citrate buffer for 30 min at 100° C. Tissue was blocked with Dako blocking solution for 1 h in a humidity chamber. Sections were labeled first with a rabbit anti-horse spleen ferritin antibody (Sigma Aldrich, St Louis, MO, USA) overnight, then labeled with donkey anti-goat Alexa 488 for 2 h followed by donkey anti-rabbit Alexa 568 (1:500; Life Technologies) for 2 h at room temperature under light protection. 4′,6-diamidino-2-phenylindole (DAPI) was applied to stain nuclei and samples were dehydrated in solutions of serially decreasing ethanol followed by histoclear. Images were obtained on a Leica confocal microscope (Leica MicroSystems, Manheim, Germany) using a 40x objective.

Statistics

We compared MRI-based measurements of N_{glom} and V_{glom} with those obtained from acid maceration and stereology using paired, two-tailed Student's t-tests at significance level α = 0.05 to test the null hypothesis that the difference of means between pairs were zero.

Acknowledgments

The authors acknowledge Amy Eggers and the Ruth Gates Lab for expertise in confocal imaging. We also gratefully acknowledge Greg Turner and Qingwei Liu of the Barrow Neurogical Institute Center for Pre-Clinical Imaging for access to MRI and lab facilities. Also, thanks to Stacey Guillot and the ACUC staff from the University of Virginia (UVa) and the UVa molecular imaging core. This work was funded by NIH DK-091722 (KB) and The Hartwell Foundation (JC).

References

1. Keller G, Zimmer G, Mall G, et al. Nephron Number in Patients with Primary Hypertension. N Eng J Med. 2002; 348:1–8.
2. Moritz KM, Wintour EM, Black MJ, et al. Factors Influencing Mammalian Kidney Development: Implications for Health in Adult Life. Adv Anat Embryol Cell Biol. 2008; 196:1–78. [PubMed: 18637522]
3. Freese A, Wehland M, Freese F, et al. Genetic low nephron number hypertension is associated with altered expression of osteopontin and CD44 during nephrogenesis. J Perinat Med. 2013; 41:295–299. [PubMed: 23241663]
4. Hayman JMJ, Johnston SM. Experiments on the relation of creatinine and urea clearance tests of kidney function and the number of glomeruli in the human kidney obtained at autopsy. J Clin Invest. 1933; 12:877–884. [PubMed: 16694171]
5. Collins AJ. Excerpts from the United States Renal Data System 2004 Annual Data Report: Atlas of end-stage renal disease in the United States. 2005; 45:A5–A7.
6. Shea SM, Raskova J, Morrison AB. A Stereologic Study of Glomerular Hypertrophy in the Subtotally Nephrectomized Rat. Am J Pathol. 1978; 90:201–210. [PubMed: 619692]
7. Gunderson HJG, Bagger P, Bendtsen TF, et al. The new stereological tools: Disector, fractionator, nucleator and point sampled intercepts and their use in pathological research and diagnosis. APMIS. 1988; 96:857–881. [PubMed: 3056461]
8. Bertram JF. Analyzing Renal Glomeruli with the New Stereology. Int Rev Cytol. 1995; 161:111–172. [PubMed: 7558690]
9. Lerch, JP.; Sled, JG.; Henkelman, RM. MRI Phenotyping of Genetically Altered Mice. In: Michos, O., editor. Kindey Dev. Vol. 711. Totowa, NJ: Humana Press; 2010. p. 349-361.
10. Bennett KM, Bertram JF, Beeman SC, et al. The emerging role of MRI in quantitative renal glomerular morphology. Am J Physiol Renal Physiol. 2013; 304:F1252–F1257. [PubMed: 23515719]

11. Xie L, Subashi E, Qi Y, et al. Four-dimensional MRI of renal function in the developing mouse. NMR Biomed. 2014; 28:546–554. [PubMed: 25810360]
12. Xie L, Dibb R, Cofer GP, et al. Susceptibility tensor imaging of the kidney and its microstructural underpinnings. Magn Reson Med. 2014; 73:1270–1281. [PubMed: 24700637]
13. Bennett KM, Zhou H, Sumner JP, et al. MRI of the basement membrane using charged nanoparticles as contrast agents. Magn Reson Med. 2008; 60:564–574. [PubMed: 18727041]
14. Beeman SC, Zhang M, Gubhaju L, et al. Measuring glomerular number and size in perfused kidneys using MRI. Am J Physiol Renal Physiol. 2011; 300:F1454–F1457. [PubMed: 21411479]
15. Heilmann M. Quantification of glomerular number and size distribution in normal rat kidneys using magnetic resonance imaging. Nephrol Dial Transpl. 2012; 27:100–107.
16. Beeman SC, Georges JF, Bennett KM. Toxicity, biodistribution, and ex vivo MRI detection of intravenously injected cationized ferritin. Magn Reson Med. 2012; 69:853–861. [PubMed: 22570266]
17. Qian C, Yu X, Chen D-Y, et al. Wireless Amplified Nuclear MR Detector (WAND) for High-Spatial-Resolution MR Imaging of Internal Organs: Preclinical Demonstration in a Rodent Model. Radiology. 2013; 268:228–236. [PubMed: 23392428]
18. Danon D, Goldstein L, Marikovsky Y, et al. Use of Cationized Ferritin as a Label of Negative Charges on Cell Surfaces. J Ultra Mol Struct R. 1972; 38:500–510.
19. Beeman SC, Cullen-McEwen LA, Puelles VG, et al. MRI-based glomerular morphology and pathology in whole human kidneys. Am J Physiol Renal Physiol. 2014; 306:F1381–F1390. [PubMed: 24647716]
20. Qian C. Sensitivity enhancement of remotely coupled NMR detectors using wirelessly powered parametric amplification. Magn Reson Med. 2012; 68:989–996. [PubMed: 22246567]
21. Grüneberg H. Genetical studies on the skeleton of the mouse XVIII. Three genes for syndactylism. J Genetics. 1956; 54:113–145.
22. Van Valen P. Oligosyndactylism, an early embryonic lethal in the mouse. J Embryol exp Morph. 1966; 15:119–124. [PubMed: 4289631]
23. Falconer DS, Latsyzewskia M, Isaacson JH. Diabetes insipidus associated with oligosyndactyly in the mouse. Gene Res. 1964; 5:473–488.
24. Zalups RK. The OS/+ mouse:a genetic animal model of reduced renal mass. Am J Physiol Renal Physiol. 1993; 264:F53–60.
25. Stewart AD, Stewart J. Studies on syndrome of diabetes insipidus associated with Oligosyndactylism in mice. American Journal of Physiology. 1969; 217:1191–1198. [PubMed: 4309975]
26. Patterson HF. In vivo and in vitro studies on the early ernhryonic lethal Oligosyndactylism (Os) in the mouse. J Embryol exp Morph. 1979; 52:115–125. [PubMed: 230280]
27. Magnuson T, Epstein CJ. Oligosyndactyly: a lethal mutation in the mouse that results in mitotic arrest very early in development. Cell. 1984; 38:823–833. [PubMed: 6091901]
28. Yee D, Golden W, Debrot S, et al. Short term rescue by RNA injection of a mitotic arrest mutation that affects the preimplantation mouse embryo. Dev Biol. 1987; 122:256–261. [PubMed: 2439395]
29. Hiraoka L, Golden W, Magnuson T. Spindle pole organization during early mouse development. Dev Biol. 1989; 133:24–36. [PubMed: 2651182]
30. Wise TL, Pravtcheva DD. Oligosyndactylism mice have an inversion of chromosome 8. Genetics. 2004; 168:2099–2112. [PubMed: 15611179]
31. Zhai XY, Birn H, Jensen KB, et al. Digital three-dimensional reconstruction and ultrastructure of the mouse proximal tubule. J Am Soc Nephrol. 2003; 14:611–619. [PubMed: 12595496]
32. Clavijo Jordan MV, Beeman SC, Baldelomar EJ, et al. Disruptive chemical doping in a ferritin-based iron oxide nanoparticle to decrease r2and enhance detection with T1-weighted MRI. Contrast Media Mol Imaging. 2014; 9:323–332. [PubMed: 24764110]
33. Charlton, JR.; Barbier, VM.; Laothamatas, I., et al. Determination of nephron number in the intact kidney: Identification of glomerular morphology by cationic ferritin does not result in renal or systemic toxicity in mice. Vancouver, Canada: 2014.

34. Beeman SC, Mandarino LJ, Georges JF, et al. Cationized ferritin as a magnetic resonance imaging probe to detect microstructural changes in a rat model of non-alcoholic steatohepatitis. Magn Reson Med. 2013; 70:1728–1738. [PubMed: 23390010]
35. Bennett KM, Zhou H, Sumner JP, et al. MRI of the basement membrane using charged nanoparticles as contrast agents. Magn Reson Med. 2008; 60:564–574. [PubMed: 18727041]
36. Shankland SJ. The podocyte's response to injury: Role in proteinuria and glomerulosclerosis. Kidney Int. 2006; 69:2131–2147. [PubMed: 16688120]
37. Dice LR. Measures of the Amount of Ecologic Association Between Species. Ecology. 1945; 26:297.
38. Amann K, Nichols C, Tornig J, et al. Effect of ramipril, nifedipine, and moxonidine on glomerular morphology and podocyte structure in experimental renal failure. Nephrol Dial Transpl. 1996; 11:1003–1011.
39. Weibel, ER. Stereological Methods, Vol 1. Practical Methods for Biological Morphometry. London: Academic Press; 1979.
40. Weibel, ER. Stereological Methods, Vol 2. Theoretical Foundations. London: Academic Press; 1979.
41. Zhong J, Perrien DS, Yang H-C, et al. Maturational regression of glomeruli determines the nephron population in normal mice. Pediatr Res. 2012; 72:241–248. [PubMed: 22717689]
42. Haas CS, Amann K, Schittny J, et al. Glomerular and renal vascular structural changes in alpha8 integrin-deficient mice. J Am Soc Nephrol. 2003; 14:2288–2296. [PubMed: 12937305]
43. Cullen-McEwen, LA.; Douglas-Denton, RN.; Bertram, JF. Estimating Total Nephron Number in the Adult Kidney Using the Physical Disector/Fractionator Combination. In: Michos, O., editor. Kidney Dev. Vol. 886. Totowa, NJ: Humana Press; 2012. p. 333-350.
44. Bonvalet J-P, Champion M, Wanstok F, et al. Compensatory Renal Hypertrophy in young rats: Increase in the number of nephrons. Kidney Int. 1972; 1:391–396. [PubMed: 4671207]

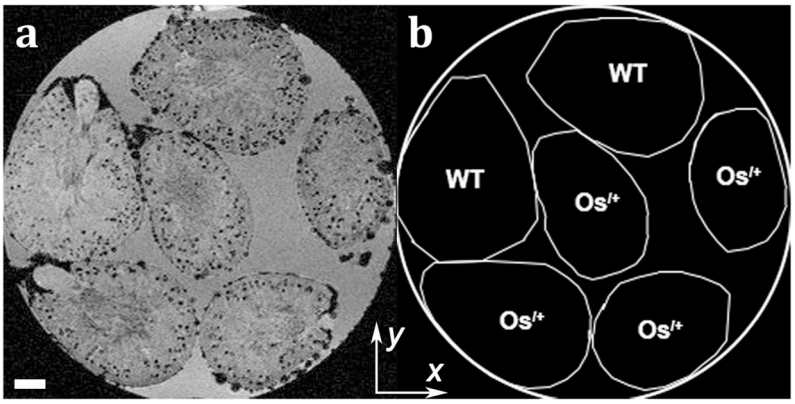

Figure 1.

Kidneys labeled with cationized ferritin (CF) were imaged together in a single 3D Magnetic Resonance Image (MRI) scan and separated in post-processing for analysis. Axial image, *A,* with its corresponding identification-maps, *B*, show clear CF labeling in all kidneys at 7 Tesla. The axial plane is defined orthogonal to the main B_0 magnetic field. Scale bar = 1mm.

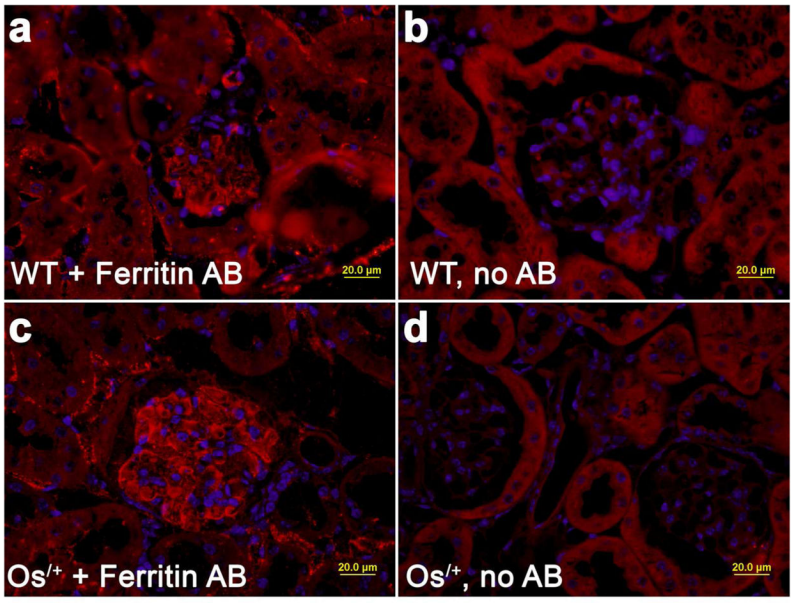

Figure 2.

Detection of cationized ferritin (CF) labeling in healthy wild type (WT) and oligosyndactylism (Os/$^{+}$) mice kidneys after retro-orbital injection using immunofluorescence (IF) imaging. Sections were stained with anti-horse spleen ferritin (AHSF) (*A* and *C*) and without AHSF (*B* and *D*). Both A and C images show fluorescence in the glomerular basement membrane (GBM), indicating CF uptake in WT and Os/$^{+}$ glomeruli. Sections that were not stained with the AHSF, *B* and *D*, showed no GBM labeling.

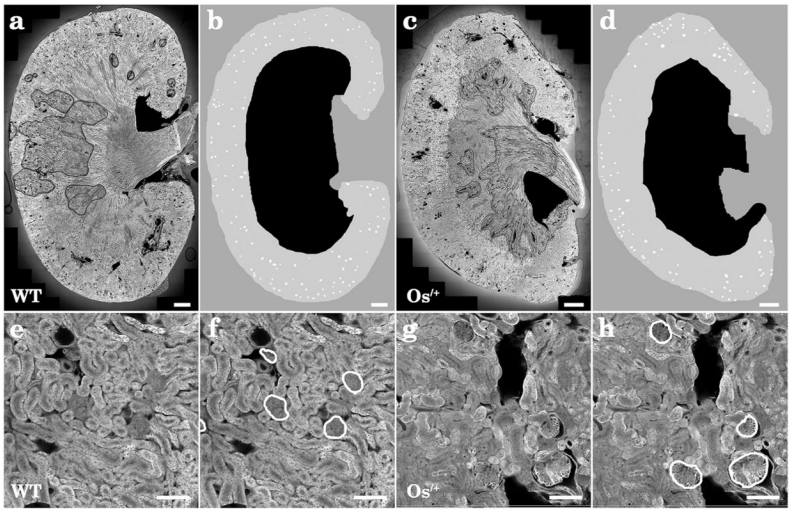

Figure 3.

Stereology was performed on kidneys imaged with magnetic resonance imaging (MRI) for direct comparison of glomerular volume and number. A and C show whole sagittal slice sections of kidneys stained with wheat germ agglutinin (WGA) in wild type (WT) and oligosyndactylism ($Os/^{+}$) mice, respectively. Glomeruli were identified in both animals (E–H). Overlayed maps (B and D) show all identified glomeruli in each section along with its cortex. It was clear during segmentation/inspection of all kidneys that $Os/^{+}$ mice had abnormally large glomerular profiles, as seen in G–H, as compared with WT, E–F. (Top row scale bars equal ~.5 mm; Bottom row scale bars equal ~.1 mm)

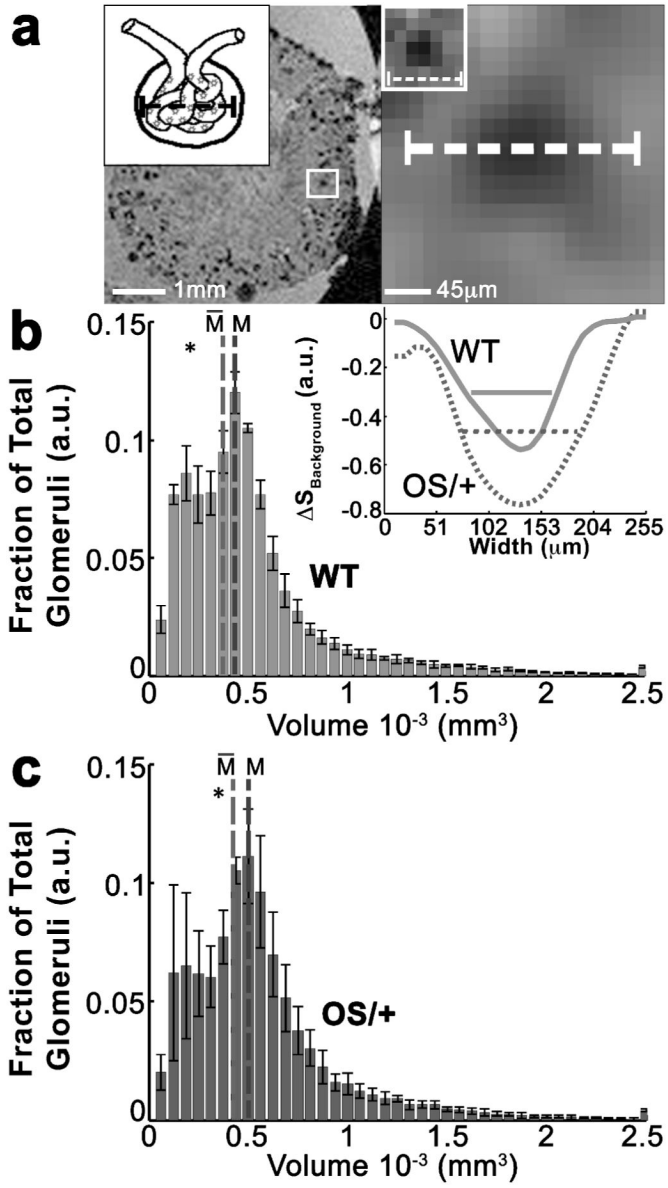

Figure 4.

Individual glomerular volumes measured with cationic ferritin enhanced magnetic resonance imaging (CFE-MRI) were calculated using line profile widths at different heights of the line profile and volumes were calculated based on the assumption that glomeruli are spherical. Widths were taken from 50%, 55%, 60%, and 75% of total profile height and corresponding volumes were calculated using the width as glomerular diameter. Full width at 55% height matched stereology the best for both wild type (WT) and oligosyndactylism (Os/$^{+}$) mice. (*A)* Top figure and inset (*B)* shows how CF labeled glomeruli in MRI before and after image resampling and how line profiles were used to measure IGV. *B* and C show the corresponding mean distribution of all calculated glomerular volumes. Both WT and OS/$^{+}$ kidneys exhibited bimodal distributions. (Symbol Meanings: M – Median Value; $\bar{M}$ – Mean Value; * - Mean Value from Stereology)

a

Label	MRI		Stereology		Acid Maceration		
	Mean N_{Glom}	Mean V_{Glom}	Mean N_{Glom}	Mean V_{Glom}	Mean N_{Glom}	Kidney Volumes	Kidney Weight
		$mm^3 \times 10^{-4}$		$mm^3 \times 10^{-4}$		mm^3	mg
WT-1	11,971	2.640	13,315	2.190	11,020	153	163
WT-2	12,740	2.521	11,625	2.298	11,690	163	168
WT-3	12,513	2.797	11,247	2.757	8,700	149	156
WT-4	11,920	2.761	10,591	2.520	10,070	145	151
WT-5	11,908	2.702	11,521	2.400	10,340	137	156
Mean	***12,210±389***	***2.684±.109***	***11,660±1,009***	***2.433±.219***	***10,364±1,123***	***149.4±9.6***	***158.8±6.7***
Os-1	4,949	3.677	3,909	3.980	3,900	111	124
Os-2	4,225	3.784	5,470	3.818	5,376	105	101
Os-3	5,671	3.239	4,704	4.517	3,820	112	89
Os-4	5,658	3.131	4,810	4.362	4,410	102	115
Os-5	7,656	2.047	8,913	2.679	3,900	113	120
Mean	***5,632±1,279***	***3.176±.389***	***5,417±1,648***	***3.871±.724***	***4,281±655***	***108.6±4.8***	***109.8±14.5***
C-1	1,085	-------	-------	-------	-------	-------	-------
C-2	1,064	-------	-------	-------	-------	-------	-------
Mean	***1,075***	-------	-------	-------	-------	-------	-------

b

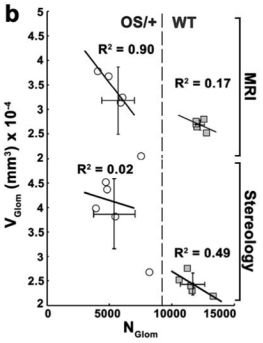

Figure 5.

A, Glomerular number (N_{glom}) and volume (V_{glom}) were measured in wild type (WT) and oligosyndactylism (Os/$^{+}$) mice kidneys by histology/stereology, acid maceration and by cationized ferritin enhanced magnetic resonance imaging (CFE-MRI). The number of glomeruli per total volume (N_V) was calculated using the formula $N_V = k/\beta \times N_A^{1.5}/V_V^{0.5}$ with constant values listed in Methods. Cortical volume (V_{Cortex}) was assessed from segmentation of 3D-MRI images based on the difference signal magnitude between cortex and medulla in MRI. The number of glomeruli per kidney (N_{glom}) was calculated by $N_{glom} = N_V \times V_{Cortex}$. V_{glom} was calculated by $V_{glom} = (V_{glom}/V_{Kidney}) / (N_{glom}/V_{Kidney})$ with V_{glom}/V_{Kidney} defined as V_V and the relation $A_A = V_V$ (V_V = Particle volume density; A_A = Particle area density; N_A = Number of glomeruli per cortex section). V_{glom} in MRI was defined from mean IGV calculated from line profiles through each identified glomerulus. Profile widths of glomeruli were measured in 3D, and glomerular volume was calculated from this width. Measurements performed with MRI agreed with estimates obtained with stereology and acid maceration. As shown in *B*, V_{glom} trends lower with increasing N_{glom} using both MRI and stereology.

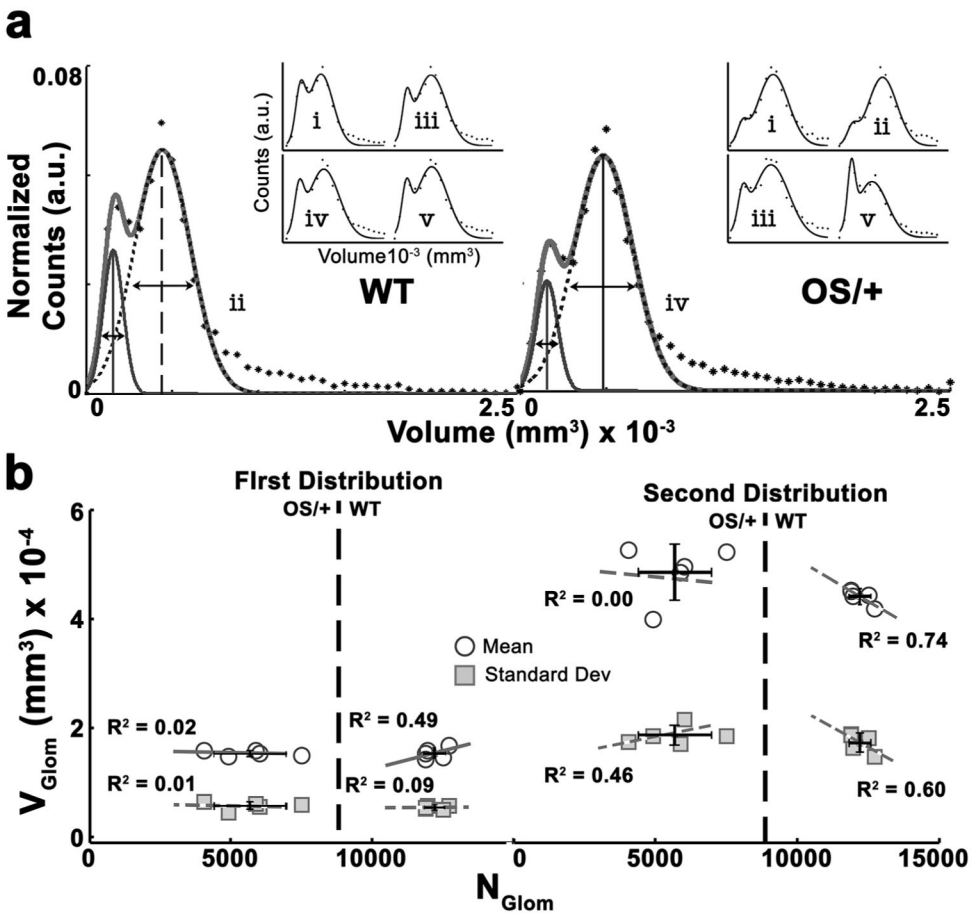

Figure 6.

Intrarenal glomerular volume distributions in all mice exhibited bimodal distributions of small ($V_{G\text{-}Low}$) and larger ($V_{G\text{-}High}$) glomeruli. *A* shows a representative data set for both wild type (WT) and oligosyndactylism ($Os/^{+}$) mice kidneys and shows an overlay of the Gaussian model with measured data. The inset also shows volume distributions for all other kidneys with the double Gaussian curve fit overlain. We obtained mean values (V_{glom}) and standard deviations (sDev-V_{glom}) from the double Gaussian model fitted to all volume distributions. *B* shows the correlations of N_{glom} with V_{glom} and N_{glom} with sDev-V_{glom} for $V_{G\text{-}Low}$ and $V_{G\text{-}High}$ in WT and $Os/^{+}$ kidneys.

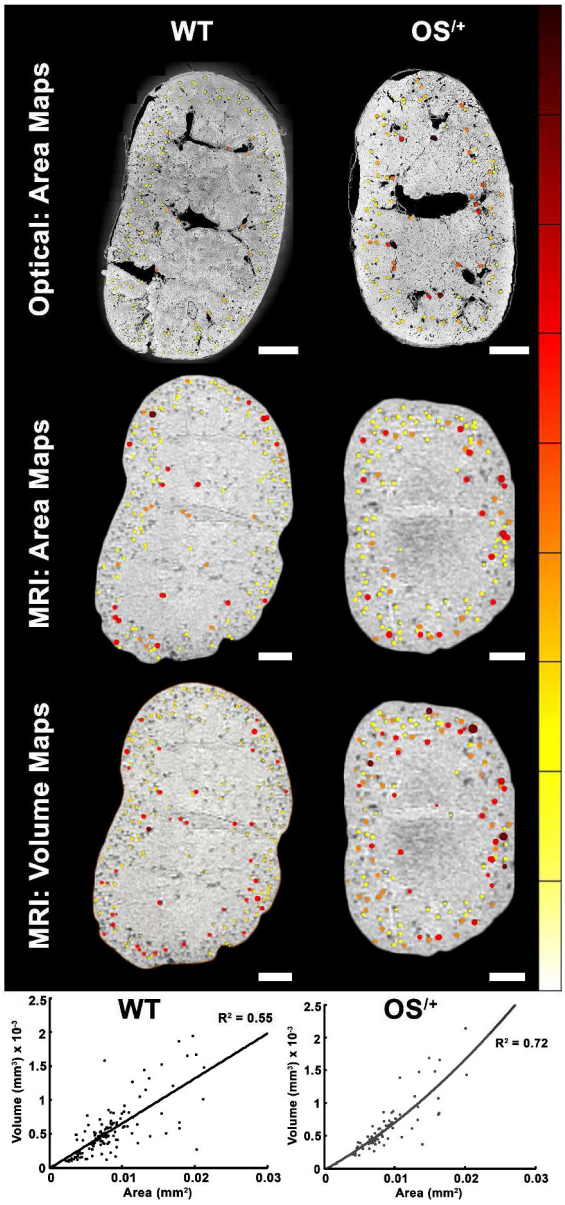

Figure 7.

Spatial distribution of glomerular size. Sagittal image slices from MRI and histological sections were taken from similar locations in wild type (WT) (Top) and oligosyndactylism (Os/$^{+}$) (Bottom) kidneys and their glomerular areas and volume profiles overlain. The areas of the profiles from both magnetic resonance imaging (MRI) and stereology images appeared larger and denser in the Os/$^{+}$ kidney compared with WT. Both MRI and stereology indicated that Os/$^{+}$ kidneys had on average larger glomeruli based on their profile area, and an increased percentage of larger glomeruli compared with the WT kidney. Individual glomerular volumes measured from glomerular centroids were calculated and rendered in 3D with the original MR dataset. As shown in the sagittal MR images with maps of the glomeruli colored by volume, the Os/$^{+}$ mice had at least a 7% larger number of glomeruli with increased volume. There was a ~ 60% correlation between MRI-based measurements of

area and volume for both WT and Os/+ kidneys using a second-order polynomial fit. Largest glomeruli were most frequently observed in the juxtamedulary areas in both WT and Os/$^{+}$ kidneys. (Scale bars equal ~ 0.5 mm)